Calculating the Optical Properties of Multidimensional Heterostructures: Application to the Modeling of Quaternary Quantum Well Lasers

D. Gershoni, C. H. Henry and G. A. Baraff

Abstract—**A method for calculating the electronic states and optical properties of multidimensional semiconductor quantum structures is described. The method is applicable to heterostructures with confinement in any number of dimensions: e.g. bulk, quantum wells, quantum wires and quantum dots. It is applied here to model bulk and multiquantum well (MQW) InGaAsP active layer quaternary lasers. The band parameters of the quaternary system required for the modeling are interpolated from the available literature. We compare bulk versus MQW performance, the effects of compressive and tensile strain, room temperature versus high temperature operation and 1.3 versus 1.55 μm wavelength operation. Our model shows that: compressive strain improves MQW laser performance. MQW lasers have higher amplification per carrier and higher differential gain than bulk lasers, however, MQW performance is far from ideal because of occupation of non-lasing minibands. This results in higher carrier densities at threshold than in bulk lasers, and may nullify the advantage of MQW lasers over bulk devices for high temperature operation.**

I. Introduction

THIS PAPER is basically concerned with calculating the optical absorption and gain spectra of some quantum well laser structures. To do so, we first need to be able to calculate their electronic states and optical properties. The paper starts by describing a method for calculating electronic band structure and optical properties of multidimensional heterostructures realized in semiconductor compounds. The method used here is based on the $\mathbf{k} \cdot \mathbf{p}$ method [1], uses envelope functions [2] and has been described in partial detail elsewhere [3]. Lattice mismatch strain, which is commonly used in heterostructures grown by modern epitaxial techniques, is incorporated into this calculation using deformation potentials [4].

Our method provides a common approach for calculating the optical properties of heterostructures with confinement in any number of dimensions, e.g., bulk semiconductors, one dimensional quantum heterostructure systems (quantum wells, multiquantum wells and superlattices), two dimensional quantum systems (quantum wires) and three dimensional systems (quantum dots). For all these systems, we provide essentially the same means of calculating the spectra of both types of optical transitions, namely, across the fundamental band-gap (interband transitions) and also within the conduction or valence band (intersubband transitions).

We apply this method to the InGaAsP/InP quaternary heterostructure system which is currently used for optical communications. Relevant earlier calculations of gain in AlGaAs/GaAs and InGaAs/GaAs active layer lasers, taking into account the valence band structure were made by Corzine *et al.* [5]. Strain effects on the valence band structure and consequently on performance of InGaAsP/InP quantum well lasers were considered by Loehr and Singh [6] and also in [5]. Our approach is more accurate in the sense that it takes into account the conduction band structure as well. It permits us also to model any shape potential structure in the active layer in one or more dimensions. We calculate miniband dispersion curves and optical matrix elements and use them to obtain gain spectra, curves of peak gain versus carrier density and threshold dependence on temperature. We compare MQW and bulk lasers, room temperature and high temperature operation, 1.3 and 1.55 μm wavelength operation lasers, and compressively strained, tensilely strained and unstrained MQW lasers. We also compare ideal and actual MQW laser performance. In this way, we try to draw conclusions about the advantages and disadvantages of quaternary MQW lasers.

The manuscript is organized as follows: In Section II we describe the theory and define the parameters needed. In Section III, we describe the software code that we have developed for the actual calculation of the multidimensional heterostructure band structure and for optical transitions between the different bands. Section IV details the calculation of optical spectra from the calculated elec-

Manuscript received October 15, 1992

D. Gershoni is with Physics Department Technion, Haifa, 32000 Israel.
C. H. Henry and G. A. Baraff are with AT&T Bell Laboratories, Murray, Hill, N.J. 07974.

IEEE Log Number 9211356.

tronic band structure and Section V lists the material constants and interpolation scheme for the InGaAsP/InP quaternary system. We conclude in Section VI by calculating optical spectral gain of bulk and quantum well quaternary lasers.

II. Theory

A. The Hamiltonian and Its Parameters

The electronic states and the energy levels of the semiconductor device are found in principle by solving the Schrödinger equation:

$$H_0\psi = \left[\frac{\mathbf{p}^2}{2m_0} + V(\mathbf{r})\right]\psi = E\psi \tag{1}$$

where H_0 is the Hamiltonian, ψ is the electronic wave function, E is the total energy, $\mathbf{p}$ is the momentum operator, $\mathbf{r}$ is the position vector, m_0 is the free electron mass and $\mathbf{V}(\mathbf{r})$ is the potential created by the atoms in the semiconductor device. This equation can be solved for the perfect spatially uniform semiconductor using a variety of well known techniques [7], but in a heterostructure or a quantum wire or dot, the crystal composition and/or strain varies from region to region and approximations are needed in order to solve equation (1). Many such approximate methods are now well known and extensively used [2], [8]–[10]. In this paper, we use the $\mathbf{k}\cdot\mathbf{p}$ method and envelope functions. This means that in each (compositionally homogeneous) region of the structure, the wave function is assumed to be of the form

$$\Psi(\mathbf{r}) = \sum_n U_n(\mathbf{r})F_n(\mathbf{r}) \tag{2}$$

where the $U_n(\mathbf{r})$ are zone center Bloch waves for the material in a particular region. The $F_n(\mathbf{r})$ are called envelope functions, and the summation is restricted to Bloch waves whose energies are close to the fundamental gap. The choice of how many functions will be needed depends on the details of the problem to be solved: For the work being reported here, it is appropriate to include eight functions in the set, namely the spin up and spin down zone center Bloch waves from the conduction band minimum, and the spin up and spin down functions from each of the three degenerate p-like states at the top of the valence band. The result of this approximation is that the Schrödinger equation is converted into a set of eight coupled differential equations for the envelope functions. The equations are ordinary differential equations for quantum wells, and partial differential equations for quantum wires and quantum dots.

These equations must be augmented by boundary conditions which describe how the envelope functions are to be joined at the boundaries of adjacent regions. Although there has been controversy associated with the question of matching conditions, we have investigated this point and, for reasons explained elsewhere [3], have accepted the usual conditions which lead to envelope function continuity and current conservation across the boundary.

The equations contain parameters: these parameters are constants in each region. Their values are determined by solving the differential equations (specialized to the form representing a bulk semiconductor) and adjusting the parameters so as to fit various experimental quantities measured in the bulk material. The quantities fitted are band gaps, band offsets, spin orbit splittings, effective masses and effective mass anisotropies in various bands. One of the parameters determined in this way has a special significance for its dual role: not only is it important in the differential equations but it also plays an important role in evaluating the matrix element for optical transitions.

Not all of the parameters are known for all the semiconductor alloys of interest. In the cases where the parameters are not known *a priori*, we have interpolated their values from the values they have in other related alloys. This will be explained later. For now, we describe the form of the coupled differential equations so as to be able to exhibit and define the parameters they depend on.

The set of eight coupled differential equations can be written in the general form

$$\sum_n H(\mathbf{r}, \mathbf{k})_{mn}F_n(\mathbf{r}) = EF_m(\mathbf{r}). \tag{3}$$

Equation (3) can be used both to obtain the band structure of a perfect semiconductor in the region of the Brillouin zone near $\mathbf{k} = 0$ for energies near the gap, and also to obtain the wave functions in the heterostructure. In a bulk semiconductor, the symbol k_j is interpreted as a component of the $\mathbf{k}$ vector that labels the Bloch waves. In the heterostructure, the symbol k_j is interpreted as the differential operator

$$k_j \rightarrow \frac{1}{i}\frac{\partial}{\partial x_j}. \tag{4}$$

The rows and columns are labeled by zone-center Bloch waves in the following order: First, the spin up Bloch wave for the conduction band, then the three for the valence band $|s\uparrow>$, $x\uparrow>|y\uparrow>|z\uparrow>$, then their time-reversed conjugates. $|s\downarrow>$, $|x\downarrow>$, $|y\downarrow>$ and $|z\downarrow>$. In this basis, the matrix H takes the form:

$$H = \begin{bmatrix} G & \Gamma \\ -\Gamma^* & G^* \end{bmatrix}, \tag{5}$$

where G and Γ are both 4×4 matrices.

We follow Kane [1] in defining the matrices $G(\mathbf{k})$ and Γ:

$$G(\mathbf{k}) = G_1(\mathbf{k}) + G_2(\mathbf{k}) + G_{so}, \quad \text{where} \tag{6}$$

$$G_1 \equiv \begin{bmatrix} E_c & iPk_x & iPk_y & iPk_z \\ -iPk_x & E_{v'} & 0 & 0 \\ -iPk_y & 0 & E_{v'} & 0 \\ -iPk_z & 0 & 0 & E_{v'} \end{bmatrix} \tag{7}$$

TABLE I
EIGENVALUES AND CORRESPONDING EIGENSTATES AT $k = 0$: THE STATES HAVE BEEN ARRANGED SO THAT EIGENSTATES IN THE SECOND SET ARE THE TIME-REVERSE CONJUGATES OF THOSE IN THE FIRST SET

Energy	First Kramers Set	Second Kramers Set	Name
E_c	$\left\|\frac{1}{2},\frac{1}{2}\right> = \|S\uparrow>$	$\left\|\frac{1}{2},\frac{-1}{2}\right> = \|S\downarrow>$	Electron
$E_v = E_v' + \frac{\Delta}{3}$	$\left\|\frac{3}{2},\frac{3}{2}\right> = \frac{1}{\sqrt{2}}[\|x\uparrow> + i\|y\uparrow>]$	$\left\|\frac{3}{2},\frac{-3}{2}\right> = \frac{1}{\sqrt{2}}[\|x\downarrow> - i\|y\downarrow>]$	Heavy Hole
$E_v = E_v' + \frac{\Delta}{3}$	$\left\|\frac{3}{2},\frac{1}{2}\right> = -\sqrt{\frac{2}{3}}\|z\uparrow> + \frac{1}{\sqrt{6}}[\|x\downarrow> + i\|y\downarrow>]$	$\left\|\frac{3}{2},\frac{-1}{2}\right> = \frac{-1}{\sqrt{6}}[\|x\uparrow> - i\|y\uparrow>] - \sqrt{\frac{2}{3}}\|z\downarrow>$	Light Hole
$E_{SO} = E_v' - \frac{2\Delta}{3}$	$\left\|\frac{1}{2},\frac{1}{2}\right> = \frac{1}{\sqrt{3}}[\|x\downarrow> + i\|y\downarrow> + \|z\uparrow>]$	$\left\|\frac{1}{2},\frac{-1}{2}\right> = \frac{-1}{\sqrt{3}}[\|x\uparrow> - i\|y\uparrow> - \|z\downarrow>]$	S.O. Hole

$$G_2 \equiv \begin{bmatrix} A'k^2 & Bk_yk_z & Bk_xk_z & Bk_xk_y \\ Bk_yk_z & L'k_x^2 + M(k_y^2 + k_z^2) & N'k_xk_y & N'k_xk_z \\ Bk_zk_x & N'k_xk_y & L'k_y^2 + M(k_x^2 + k_z^2) & N'k_yk_z \\ Bk_xk_y & N'k_xk_z & N'k_yk_z & L'k_z^2 + M(k_x^2 + k_y^2) \end{bmatrix} \tag{8}$$

and

$$G_{so} = -\frac{\Delta}{3}\begin{bmatrix} 0 & 0 & 0 & 0 \\ 0 & 0 & i & 0 \\ 0 & -i & 0 & 0 \\ 0 & 0 & 0 & 0 \end{bmatrix} \tag{9}$$

The matrix Γ is

$$\Gamma = -\frac{\Delta}{3}\begin{bmatrix} 0 & 0 & 0 & 0 \\ 0 & 0 & 0 & -1 \\ 0 & 0 & 0 & i \\ 0 & 1 & -i & 0 \end{bmatrix} \tag{10}$$

All the parameters appearing in (7)–(10) are real. The parameters A', B, L', M, and N' are defined in Kane's article in terms of $\mathbf{k} \cdot \mathbf{p}$ perturbation sums over all bands other than the eight we consider. The parameter B, which is equal to zero for crystals with inversion symmetry, is set to zero in our calculations as well. The parameter P is proportional to the momentum matrix element between the conduction band and the valence band.

$$P \equiv -i\frac{\hbar}{m_0}\langle s|p_x|x\rangle \tag{11}$$

It is also known as the optical matrix element. It plays a role in calculating the optical transition strength. The quantity Δ is the spin orbit splitting parameter, while E_c and $E_{v'}$ are the band edge energies in the absence of the spin-orbit coupling.

To obtain the material parameters from the experimentally measured properties of the bulk semiconductor crystal, one considers the components of the $\mathbf{k}$ vector in matrix (5) to be numbers, and diagonalizes the matrix to get the dispersion relationship, namely, the $\mathbf{k}$ dependent eigenvalues $E_n(\mathbf{k})$. The derivatives of this dispersion relationship are effective masses, and the values of the energies at $\mathbf{k} = 0$ are the (experimental) band edges.

The matrix (5) can be solved exactly for $\mathbf{k} = 0$. The eigenvalues and eigenstates for this case are listed in Table I. The band edge effective masses are defined by

$$\left(\frac{1}{m_n^*}\right)_{ij} = \frac{1}{\hbar^2}\frac{\partial^2 E_n(\mathbf{k})}{\partial k_i\,\partial k_j}. \tag{12}$$

Solving the dispersion relation to second order in $\mathbf{k}$ allows one to obtain

$$\frac{m_0}{m_{hh}(100)} = \gamma_1 - 2\gamma_2 \qquad \frac{m_0}{m_{lh}(100)} = \gamma_1 + 2\gamma_2 \tag{13a}$$

$$\frac{m_0}{m_{hh}(111)} = \gamma_1 - 2\gamma_3 \qquad \frac{m_0}{m_{lh}(111)} = \gamma_1 + 2\gamma_3 \tag{13b}$$

$$\frac{m_0}{m_{el}} = \frac{2m_0}{\hbar^2}\left(A' + \frac{P^2(E_g + \frac{2}{3}\Delta)}{E_g(E_g + \Delta)}\right) \tag{13c}$$

$$\frac{m_0}{m_{so}} = \gamma_1 - \frac{2m_0P^2\Delta}{3\hbar^2E_g(E_g + \Delta)} \tag{13d}$$

where $m_{hh(lh)}(ijk)$ is the heavy (light) hole band edge effective mass in the (ijk) crystallographic direction, m_{el} is the conduction band effective mass and m_{so} is the split-off band effective mass. The γ_i are known as the Luttinger parameters [11]. We use them here in order to facilitate simple comparison with parameters from the available literature. In terms of the γ_i, the constants in the matrix are given by

$$L' = -\frac{\hbar^2}{2m_0}(1 + \gamma_1 + 4\gamma_2) + \frac{P^2}{E_g}$$

$$M = -\frac{\hbar^2}{2m_0}(1 + \gamma_1 - 2\gamma_2)$$

$$N' = -\frac{3\hbar^2}{m_0}\gamma_3 + \frac{P^2}{E_g} \tag{14}$$

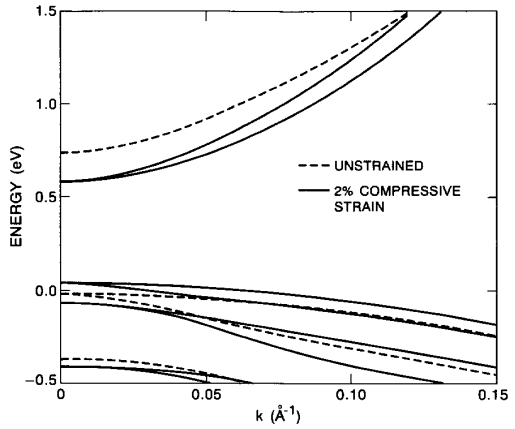

Fig. 1. Band diagram of bulk 1.55 μm laser material (dashed lines). Bands after 2% compressive strain (solid lines).

TABLE II
MATERIAL CONSTANTS

Constant	GaAs	InAs	InP	$In_{0.532}Ga_{0.468}As$
E_g(300°K) eV	1.424[a]	0.354[a]	1.351[a]	0.75[b]
Δ_0 eV	0.341[a]	0.371[a]	0.110[a]	0.356[c]
m_e^*(e.m.u)	0.0665[a]	0.023[a]	0.079[a]	0.041[c,d]
γ_1	6.790[e]	19.67[g]	4.95[a]	11.01[d]
γ_2	1.924[e]	8.37[g]	1.65[a]	4.18[d]
γ_3	2.782[g]	9.29[g]	2.35[a]	4.84[d]
a_g (eV)	−9.77[a]	−6.0[a]	−6.35[a]	−7.76[c]
a_c (eV)	−7.1[h]	−5.4[h]	−5.35[b]	−6.2[c]
b_v (eV)	−1.7[a]	−1.8[a]	−2.0[a]	−1.75[c]
d_v (eV)	−4.55[a]	−3.6[a]	−4.2[a]	−4.04[c]
E_p(eV)	28.8[i]	22.2[g]	20.4[g]	25.3[c,d]
C_{11} ($\times 10^{10}$ dyn/cm^2)	11.81[d]	8.329[d]	10.22[d]	10.08[c]
C_{12} ($\times 10^{11}$ dyn/cm^2)	5.38[d]	4.53[d]	5.76[d]	4.98[c]
C_{14} ($\times 10^{11}$ dyn/cm^2)	5.94[d]	3.96[d]	4.60[d]	4.89[c]
a(300°K) Å	5.6532[d]	6.0583[d]	5.8587[d]	5.8687[c]
V of relative to InP	0.34	0.41	0	0.37

[a] *Semiconductors*, eds. O. Modeling, M. Schulz and H. Weiss, Landolt-Börstein New Series, Group 3, vol. 17a (Springer, Berlin, 1982).
[b] R. E. Nahory, M. A. Pollack, W. D. Johnston, Jr., and R. L. Borus, *Appl. Phys. Lett.* vol. 33, pp. 659-651, 1978.
[c] Linearly interpolated from the binary parents constants.
[d] K. Alavi and R. L. Aggrawal, *Phys. Rev.* vol. B21, 1980, p. 1311.
[e] D. F. Nelson, R. C. Miller and D. A. Kleinman, *Phys. Rev.*, vol. B35, 1987, p. 7770.
[f] D. Gershoni et al. *Phys. Rev. B.*
[g] P. Lawaetz, *Phys. Rev.* vol B4 p. 3960 (1971) calculated.
[h] D. L. Camphansen, G. A. Nevill Connel and W. Paul, *Phys. Rev. Lett.* vol. 26, 1971, p. 184?.
[i] Hermann and C. Weisbuch, *Phys. Rev.* vol. B15, p. 823, 1977.
[j] S. Adachi, *J. Appl. Phys.* vol. 53, p. 12, 1982.

where $E_g = E_c - E_v$ is the band gap with $E_v = E_{v'} + \Delta/3$. The mathematical relations (13)–(14) define all the 8×8 Hamiltonian parameters in terms of the experimental bandgap, effective masses and the spin orbit splitting. Note that if P is known from experiment, then the knowledge of the spin-orbit split-off band effective mass is not necessary and vice versa.

In Fig. 1, we illustrate the band structure of 1.55 μm InGaAsP quaternary lattice matched to InP using the parameters listed in Table II. The dashed lines represent the band structure for the unstrained lattice.

B. Strain in Bulk Semiconductors

The $\mathbf{k} \cdot \mathbf{p}$ 8×8 bulk Hamiltonian described by equations (9)–(14) acquires extra terms when the crystal is strained. These extra terms can be obtained by repeating the original derivation given by Pikus and Bir [12] using Kane's formalism [1] as has been recently done by Bahder [13]. The strain interaction couples only parallel spins and hence this interaction adds an additional term G_{strain} to the Hamiltonian H in (5).

The additional matrix is:

$$G_{\text{strain}} = \begin{bmatrix} a_c[e_{xx} + e_{yy} + e_{zz}] & b'e_{yz} - iP\Sigma_j e_{xj}k_j & b'e_{zx} - iP\Sigma_j e_{yj}k_j & b'e_{xy} - iP\Sigma_j e_{zj}k_j \\ b'e_{yz} + iP\Sigma_j e_{xj}k_j & le_{xx} + m(e_{yy} + e_{zz}) & ne_{xy} & ne_{xz} \\ b'e_{zx} + iP\Sigma_j e_{yj}k_j & ne_{xy} & le_{yy} + m(e_{xx} + e_{zz}) & ne_{yz} \\ b'e_{xy} + iP\Sigma_j e_{zj}k_j & ne_{xz} & ne_{yz} & le_{zz} + m(e_{xx} + e_{yy}) \end{bmatrix} \tag{15}$$

where e_{ij} are the strain tensor components. The constants l, m, and n are related to the material deformation potentials by:

$$a_v = \frac{1}{3}(1 + 2m): \quad b_v = \frac{1}{3}(1 - m) \quad \text{and} \quad d_v = \frac{1}{\sqrt{3}}n \tag{16}$$

where a_c is the conduction band hydrostatic deformation potential, a_v is the valence band hydrostatic deformation potential, b_v is the valence band shear deformation potential associated with strain along the (100) crystallographic direction and d_v is the shear deformation potential for strain along the (111) direction. Most of the deformation potentials can be measured by applying stress on a crystal. Note, however, that experiments usually measure the band gap hydrostatic deformation potential $a_g = a_c - a_v$ and additional information is needed in order to determine the individual band hydrostatic deformation potential a_c or a_v [14]. In our calculations we set $b' = 0$ since this value agrees with the available experimental data.

In Fig. 1, the solid lines represent the band structure of 1.55 μm InGaAsP quaternary subject to 2% biaxial strain in the (001) plane. Note that the band edges move relative to the unstrained quaternary, and that the degeneracy between the light and heavy hole at $\mathbf{k} = 0$ is removed. Each state of the quantum system is still doubly degenerate, due to time reversal degeneracy, although an additional

degeneracy that used to be present (between two states having the same value of **k** vector) is removed by the tetragonal distortion of the cubic lattice caused by the strain.

C. Electronic States of Semiconductor Heterostructures

The heterostructure is composed of several regions, each of a definite composition and/or uniform state of strain. In such a situation, the parameters in the Hamiltonian matrix (5) are constants in each region but differ from region to region. Also in such a situation, the question of how to match the envelope functions in one region to those in the next region arises. We have studied this problem elsewhere [3] and have found a simple prescription for automatically including the correct boundary conditions into the formulation of the problem. That prescription is as follows: In every term of (7) and (8) in which a material parameter and a derivative both appear, one is to make the replacement

$$Q\frac{\partial}{\partial x_\mu} \rightarrow \frac{1}{2}\left[Q(\mathbf{r})\frac{\partial}{\partial x_\mu} + \frac{\partial}{\partial x_\mu}Q(\mathbf{r})\right]$$

$$Q\frac{\partial}{\partial x_\mu}\frac{\partial}{\partial x_\nu} \rightarrow \frac{1}{2}\left[\frac{\partial}{\partial x_\mu}Q(\mathbf{r})\frac{\partial}{\partial x_\nu} + \frac{\partial}{\partial x_\nu}Q(\mathbf{r})\frac{\partial}{\partial x_\mu}\right] \quad (17)$$

where $Q(\mathbf{r})$ is any real material parameter or stain tensor component.

The spatial dependence of the parameters $Q(\mathbf{r})$ is expressed in terms of step functions for the interfaces i.e., for an interface at $x = x_0$ where material A is to the left side of the interface and material B is to the right side:

$$Q(x) = Q_A + (Q_B - Q_A)\Theta(x - x_0) \quad (18a)$$

where

$$\Theta(x - x_0) = \begin{cases} 0 & x < x_0 \\ 1 & x \geq x_0. \end{cases} \quad (18b)$$

The action of the derivative operator on the step function is to produce a delta function. The delta functions are to be retained in the elements of H_{mn}. Their role is to impose the correct slope-discontinuity boundary conditions on a solution which is treated as being otherwise continuous. (Later, when we employ Fourier series to evaluate the solution, many terms will be needed to accurately reproduce these slope discontinuities. In practice, the optical matrix elements and the optical transition energies are given with sufficient accuracy well before the slope discontinuity itself is precisely depicted. It is this feature that makes the method a practical one.)

The 8×8 matrix obtained in this way has elements $H_{nn'}(\mathbf{r}, \nabla)$ and the eight coupled differential equations are

$$\sum_{n'=1}^{8} H_{nn'}(\mathbf{r}, \nabla)F_{n'}(\mathbf{r}) = EF_n(\mathbf{r}). \quad (19)$$

These equations must now be solved. The easiest way we have found to do this is to expand the envelope functions $F_n(\mathbf{r})$ is a discrete Fourier series, and then to convert (19) to a giant algebraic set of coupled equations for the Fourier coefficients. We use a one, two- or three-dimensional Fourier series according to whether the structure has spatial variation in one, two, or three dimensions. As example, where all three dimensions are needed, the expansion would take the form

$$F_n(\mathbf{r}) = \sum_{jlm}^{\infty} F_n(jlm)\phi_{jlm}(xyz) \quad (20a)$$

where:

$$\phi_{jlm}(xyz) = (XYZ)^{-1/2}\exp\left[2\pi i\left(j\frac{x}{X} + l\frac{y}{Y} + m\frac{z}{Z}\right)\right]. \quad (20b)$$

The $F_n(jlm)$ are complex numbers. A *discrete* Fourier series assumes that the overall structure is periodic with period X, Y, and Z along the x, y, and z directions respectively. In some cases, this is exactly what is wanted. In other cases, one would like to solve for only a single isolated heterostructure. In that case, one must choose X, Y, and Z to be large enough relative to the actual size of the structure that the periodic replicas of this structure do not interact with each other. We shall return to this point later.

In order to convert the differential (19) into a set of algebraic equations, we insert the expansion (20) into (19), multiply by $\phi^*_{jlm}(xyz)$ and integrate over the region XYZ. The resultant matrix eigenvalue equation has the form:

$$\sum_{n'j'l'm'} H_{nn'}(j', l', m', j, l, m)F_{n'}(j'l'm') = EF_n(j, l, m) \quad (21)$$

where the matrix elements $H_{nn'}(j', l', m', j, l, m)$ are given by:

$$H_{nn'}(j', l', m', j, l, m) = \int dx\,dy\,dz\,\phi^*_{j'l'm'}(xyz)H_{nn'}(\mathbf{r}, \nabla)\phi_{jlm}(xyz). \quad (22)$$

All matrix elements can be evaluated analytically if each interface is perpendicular to one or another coordinate axis.

The number of interfaces that can be taken into account is not limited by this procedure, and in practice, a larger number of interfaces will only increase the computation time needed to form the matrix H. However, once formed, the time required to diagonalize the matrix (which is the most time consuming step) does not depend on the number of interfaces. By dividing space into many piecewise continuous regions, any spatial dependence of the parameters $Q(\mathbf{r})$ can be approximated.

When constructing the matrix H, there are two useful checks on the numerical work. The first check is that the matrix H is Hermitian:

$$H_{nn'}(j', l', m', j, l, m) = H_{n'n}(j, l, m, j', l', m')^*. \quad (23)$$

The second check is that the matrix H expressed in a Kramers basis [a basis containing $2N$ functions arranged so

that the $(j + N)$-th function is the time-reverse conjugate of the jth function] must also have the form (5). In constructing the Kramers basis for the matrix H, we note that the original 8-function basis is a Kramers basis and that $\phi_{-j,-l,-m}(xyz)$ is the time reverse conjugate of $\phi_{jlm}(xyz)$.

We have assumed so far that the coordinates describing the geometry of the heterostructure refer to axes which coincide with the crystallographic axes of the underlying crystal. When evaluating heterostructures or strained regions which are not oriented parallel to the main crystallographic axes [3], it is necessary to define a rotated coordinate system, x', y', z', to describe the heterostructure. In this case, we expand the envelope functions in a Fourier series $\phi_{jlm}(x'y'z')$ and derive the appropriate differential equations by introducing the corresponding propagation vector: $k'_\mu \rightarrow (1/i)(\partial/\partial x'_\mu)$, and specifying the rotation that expresses k in terms of k'

$$k_\mu = \sum_\nu a_{\mu\nu} k'_\nu. \tag{24}$$

We then substitute (24) into (17) and (18), drop the primes and proceed as explained before. In this case, however, one needs to recall that, although the envelope wave functions are oriented in accordance with the heterostructure axes, the Bloch wave functions are defined as before, in accordance with the coordinate system of the underlying crystal.

When dealing with a single quantum structure with *confined* states, use of the discrete Fourier series and the repeated periodic array of heterostructures it represents does not cause a problem, because the dimensions of the super cell can be chosen large enough so that the eigenstates and eigenfunctions do not depend on the cell dimensions. The wave functions from one structure do not overlap those of the next, and the spectrum is discrete. The need to use a large unit cell in this situation may be considered to be a slight disadvantage. However, use of a discrete Fourier series has a great advantage in the case of a superlattice quantum structure. Such a structure has periodicity in one or more dimensions, and the wavefunction in each unit super cell overlaps with wavefunctions in other cells. Hence, the energy spectrum is made up of minibands. The states for such a periodic system will be labeled with a band index n, which corresponds roughly to the discrete states for the corresponding single quantum structure, and with a continuous index $\mathbf{q}$, which is a propagation vector in the mini-Brillouin zone corresponding to the super unit cell. The wave functions having a given $\mathbf{q}$ value can be found by replacing the expansion functions (2.20b) according to

$$\begin{aligned}\phi_{jlm}(xyz) &\rightarrow \phi_{j+q_x, l+q_y, m+q_z}(xyz) \\ &= (XYZ)^{-1/2} \exp\left[2\pi i\left(j + q_x\right)\frac{x}{X}\right. \\ &\quad \left. + (l + q_y)\frac{y}{Y} + (m + q_z)\frac{z}{Z}\right]\end{aligned} \tag{25}$$

where $-(1/2) < q_x, q_y, q_z < 1/2$. By evaluating the energy spectrum for different values of $\mathbf{q}$, the miniband structure of the superlattice can be evaluated.

D. Optical Transitions Between Electronic States

After the states and energies of the semiconductor heterostructure system have been calculated via the method described in the previous sections, optical transitions between the states can then be evaluated. For this purpose one needs to consider the interaction of the radiation field with the carriers. This interaction is described quantum mechanically in terms of the vector potential $\mathbf{A}$. The vector potential is related to the field $\mathbf{E}$ by:

$$\mathbf{E} = -\frac{1}{c}\frac{\partial \mathbf{A}}{\partial t} \tag{26}$$

$$\mathbf{A} = \mathbf{A}_o \cos \omega t = \frac{\mathbf{A}_o}{2}\left(e^{i\omega t} + e^{-i\omega t}\right). \tag{27}$$

The interaction with radiation is found by replacing $\mathbf{p}$ in the starting Hamiltonian (2.1) by $\mathbf{p} + (e/c)\mathbf{A}$, where e is the magnitude of the electron charge. Expanding the altered term $(\mathbf{p} + (e/c)\mathbf{A})^2$, neglecting $\mathbf{A}^2$, and assuming that the $\mathbf{E}$ field is transverse (which allows us to write $\mathbf{p} \cdot \mathbf{A} = \mathbf{A} \cdot \mathbf{p}$), we get a perturbation Hamiltonian $H = H_{\text{rad}}$, where

$$H_{\text{rad}} = \frac{e}{m_o c}\mathbf{A} \cdot \mathbf{p} = \frac{e}{2m_o c}\mathbf{A}_o \cdot \mathbf{p}\left(e^{i\omega t} + e^{-i\omega t}\right). \tag{28}$$

The term $e^{i\omega t}$ induces upward transitions while the term $e^{-i\omega t}$ induces downward transitions. Both rates can be calculated (as explained below) by Fermi's golden rule [15]. (Note: The assumption of a transverse $\mathbf{E}$ field would be exact in free space. In the heterostructure laser where the dielectric constant is spatially dependent, this assumption is no longer strictly valid, but the error produced is negligible for typical laser structures, and especially so for TE polarized modes.)

For evaluating the transition rate between initial state $\Psi_i(\mathbf{r})$ and final state $\Psi_f(\mathbf{r})$ of the unperturbed Hamiltonian, one needs to calculate the term:

$$|\langle \Psi_f(\mathbf{r})|H_{\text{rad}}|\Psi_i(\mathbf{r})\rangle|^2 = \mathbf{A}_o^2\left(\frac{e}{2m_o c}\right)^2 M_{f,i}. \tag{29}$$

$M_{f,i}$ is known as the optical matrix element and it is given by:

$$M_{f,i} = |\langle \psi_f(\mathbf{r})|\hat{e} \cdot \frac{\hbar}{i}\nabla|\psi_i(\mathbf{r})\rangle|^2 \tag{30}$$

where $\hat{e}$ is a unit vector in the direction of the electric field of the radiation. We note here that our approach is general enough so that i and f may both be with the valence band, (intravalence band transition), condition band (intraconduction band transition) or one may belong to the valence band and the other to the conduction band (interband tran-

sition). We now explicitly substitute

$$\psi_{i,f}(\mathbf{r}) = \sum_{n=1}^{8} F_n^{i,f}(\mathbf{r})U_n(\mathbf{r}) = \sum_{n=1}^{8}\sum_{jlm} F^{i,f}(jlm)\phi_{jlm}(xyz)U_n(\mathbf{r}) \tag{31a}$$

into (30):

$$M_{f,i} = \left| \sum_{n,n'=1}^{8}\sum_{jlm}\sum_{j'l'm'} F_n^{f*}(jlm)F_{n'}^{i}(j'l'm') \cdot \int \phi_{jlm}^{*}(xyz)U_n^{*}(\mathbf{r})\hat{e} \cdot \nabla\phi_{j'l'm'}(xyz)U_{n'}(\mathbf{r})\, dx\, dy\, dz\, dr \right|^2. \tag{31b}$$

If we make use of the fact that the envelope functions vary relatively slowly over regions the size of a unit cell, then we can write the integral in (31b) as

$$\begin{aligned}\int \phi_{jlm}^{*}(xyz)U_n^{*}(\mathbf{r})\hat{e} \cdot \nabla\phi_{j'l'm'}(xyz)U_n(\mathbf{r})\, dr\, dx\, dy\, dz \\ \cong \int \phi_{jlm}^{*}(xyz)\phi_{j'l'm'}(xyz)\, dx\, dy\, dz \cdot \int_{\Omega(xyz)} U_n^{*}(\mathbf{r})\hat{e} \cdot \nabla U_{n'}(\mathbf{r})\, d\mathbf{r} \\ + \int \phi_{jlm}^{*}(xyz)\hat{e} \cdot \nabla\phi_{j'l'm'}(xyz)\, dx\, dy\, dz \cdot \int_{\Omega(xyz)} U_n^{*}(\mathbf{r})U_{n'}(\mathbf{r})\, d\mathbf{r}.\end{aligned} \tag{32}$$

The first integral over $\Omega(xyz)$ in (32) is actually a sum of three integrals, each one being multiplied by a component of $\hat{e}$. Each of the three is proportional to the optical matrix P or else vanishes unless n, n', and the component of ∇ are related in a very specific way. (In particular, for the element not to vanish, both n and n' must refer to the same direction of spin, n must be in the conduction band while n' must be in the valence band or vice versa, and finally the component of ∇ must be the same as the label (x, y, z) of the valence band state). The second integral over $\Omega(xyz)$ is the overlap of two Bloch waves. It vanishes unless $n = n'$.

A very useful approximation in evaluating (32) is to assume that the value of the parameter P (whose actual variation from one region of the structure to another is typically of the order of 10% or so) is independent of position so that the first integral over $\Omega(xyz)$ in (32) does not depend on (xyz). Doing so allows the remaining integrals over the ϕ functions to be evaluated analytically, making use of the fact that they are mutually orthonormal.

III. Computation

In this section we describe the software code which was written in order to numerically calculate absorption and spectral gain of the semiconductor heterostructure system.

A. Computing Energies and States

We solve the heterostructure problem described in the previous sections by diagonalizing the large matrix $H_{nn'}(j', l', m', j, l, m)$ as given by (21) and (22). This matrix is complex and Hermitian. The actual diagonalization is done by calling the appropriate subroutines from EISPACK [16]. Although the most time consuming part of the numerical solution to the problem is the matrix diagonalization, it is the easiest step in writing the software code. The important steps in the software package are actually those involved in constructing the matrix to be diagonalized.

In the first step, the user defines the heterostructure, i.e., specifies the material parameters and actual dimensions for each spatial zone. A checkerboard like heterostructure with stepwise continuous semiconductor constants is defined in space.

In the second step, the user must specify the number of waves to be used in each direction. (In the actual numerical solution, the series (20) can contain only a finite number of waves.) Obviously, the number depends on how much the material parameters vary along each dimension. Variation across a boundary sets up slope discontinuities, and these discontinuities are the most slowly convergent features of the solution. Convergence of eigenvalues and eigenstates is checked by rerunning with increased number of waves. For any direction in which the structure is uniform, only one wave is needed. The $(\mathbf{k} + \mathbf{q})$ vector of that wave is a valid quantum label for the states.

Although the software is written a general way to solve heterostructures in three dimensions (quantum dots), two dimensions (quantum wires), one dimension (quantum wells) and zero dimensions (bulk), the examples given in the rest of this paper are for the last two cases only. We concentrate on quantum wells. The generalization to the other cases are straight-forward and differ only in the amount of computing time needed to diagonalize the multi-dimensional problem.

Let us denote the one dimensional heterostructure axis by x, and call the length of the heterostructure X. Then (20) is expressed as:

$$F_n(x) = \sum_{j=-J}^{J} F_n(j)\phi_j(x)e^{i(k_y y + k_z z)} \tag{33}$$

where J is the highest term in the Fourier expansion and $\phi_j(x) = \exp[2\pi i(j(x/X))]$. The transverse wave numbers k_y and k_z can be arbitrary: there is no need to establish a Fourier periodicity in any direction where the heterostructure is spatially uniform. When the differential operators k_y and k_z in H act on the transverse exponentials, the result, using (4), is to replace those operators by the *numbers* k_y and k_z. After this step, the transverse exponentials can be removed from the equations completely. For the case of the one dimensional heterostructure, the matrix (22) will then be expressed as

$$H_{nn'}(j'j, k_y, k_z) = \int_0^X dx\, \phi_{j'}^{*}(x)H_{nn'}\left(x, k_y k_z, \frac{\partial}{\partial x}\right)\phi_j(x). \tag{34}$$

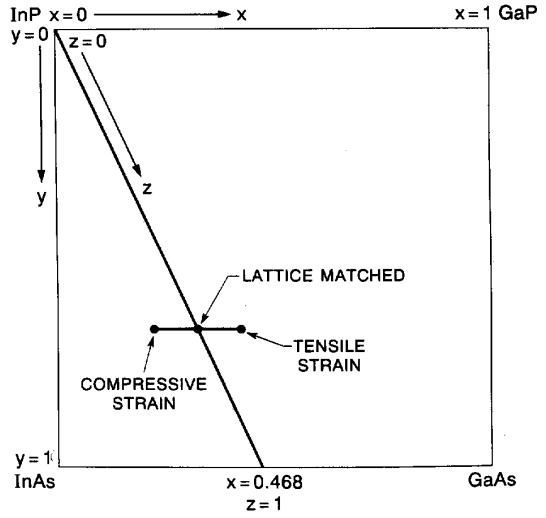

Fig. 2. Diagram of the quaternary system showing the lattice matched composition and the compositions of compressive and tensile strain.

The integral in (34) extends over all spatial regions. In each region, the material parameters are constant. The integrand also contains delta functions at each internal interface. The strength of these delta functions is governed by the discontinuity of material parameters at the interface. There are thus two types of terms contained in (34): bulk terms (integrals over the interior of the region), and surface terms (the delta-function parts). The contributions of each region and of each internal interface are additive. The program calculates the matrix elements region by region, and interface by interface, and adds them together.

All the bulk contributions to the matrix elements contain integrals of the form:

$$I^R_{j'j} = \frac{1}{X}\int_{R_L}^{R_R} dx\, e^{-ij'(x/X)} \cdot e^{ij(x/X)} \tag{35}$$

where R_L is the left side edge of the zone R and R_R is its right side. These integrals are given analytically by:

$$I^R_{j'j} = \begin{cases} \dfrac{R_R - R_L}{X} & j = j' \\ \dfrac{i}{(j'-j)}\left(\exp i\dfrac{(j-j')R_R}{X} - \exp i\dfrac{(j-j')R_L}{X}\right) & j \neq j' \end{cases} \tag{36}$$

Since the operators $H_{n'n}(x, k_y, k_z, \partial/\partial x)$ contains only constants and first- and second-order derivatives, all bulk contributions to the matrix elements in (34) can be expressed as sums of integrals of the form (36), each integral being multiplied by some material constant. The surface terms have an equally simple analytic structure. One of the useful features of this technique is that, even in two and three dimensions, the form of the elements of H_{mn} also involve only sums over products of functions of the form (35) or (36). This reduces enormously the number of separate terms that must be evaluated.

After completing the construction of the matrix (34) it is diagonalized using the appropriate subroutines from EISPACK. All the eigenvalues and eigenstates within a user defined energy range are stored for later use. Then a new k_y, k_z point is chosen and the whole procedure is repeated to complete the computation of a set of dispersion curves, such as given by Fig. 1.

B. Computation of the Optical Matrix Element

In order to calculate absorption and gain, one needs to evaluate the optical matrix element (31b). This element is absolutely straightforward to evaluate if the approximation of ignoring the spatial variation of the optical matrix element P is made, because in that case, evaluation of (32) is trivial. We have done this. We have found that, because the spatial integral of the gradient of the envelope functions is small for slowly varying envelope functions, the first of the two terms in (32) is the dominant one. Interestingly, we find that this is so for *intersubband* transitions as well as for interband transitions.

IV. Optical Spectra

A. Formula of the Spectral Gain

The power in an optical waveguide with gain grows exponentially as $e^{g_{\text{mode}}z}$, where g_{mode} is the mode gain and z is the direction of propagation. An expression for gain can be derived starting from Poynting's theorem relating the energy flux $\mathbf{S}$ to the rate of energy dissipation Q.

$$\nabla \cdot \bar{\mathbf{S}} + Q = 0 \tag{37}$$

$\bar{\mathbf{S}} = c\overline{\mathbf{E} \times \mathbf{H}}/4\pi$ is the Poynting vector in Gaussian units and the bar represents a time average. Integrating this equation over a thin volume bounded by planes at z and at $z + dz$, dividing by dz, then using the fact that $\mathbf{S}$ is growing exponentially at rate g_{mode}, we find

$$\frac{\partial}{\partial z}\int S\, da = g_{\text{mode}}\int S\, da = -\int Q\, da = -Q_{\text{act}}A_{\text{act}}. \tag{38}$$

The last equality follows because dissipation (or power generation) only occurs in the active layer whose area is A_{act}. This equation defines Q_{act} as being the average dissipation (or power generation) in the layer.

It is convenient to calculate g_{mode} in terms of g_{act}, the local gain in the active layers. This is the gain that would occur in *a uniform* active medium having the same optical properties as the quantum wells. For the same field strength as in the active layer, this medium will have the same value of power generation $-Q_{\text{act}}$. For such a medium, $g_{\text{mode}}\int S\, da$ in (38) becomes $g_{\text{act}}S_{\text{act}}A_{\text{act}}$ and (38)

reduces to

$$g_{act} S_{act} = -Q_{act}. \tag{39}$$

Substituting the expression for the Poynting vector into (39) and using $|\mathbf{E}| = n_{act}|\mathbf{H}|$, where n_{act} is the refractive index of the active medium, we find that the gain in the active material is

$$g_{act} = -\frac{4\pi Q_{act}}{n_{act} c \overline{\mathbf{E}^2}} \tag{40}$$

where c is the velocity of light.

We can find Q by considering the interaction of the radiation and the carriers. The rate of either upward or downward optically induced transitions between a state in the mini-conduction band $|c(\mathbf{k})>$ and a state in the mini-valence band $|v(\mathbf{k})>$ is given by time dependent perturbation theory (Fermi's golden rule) using H_{rad} (28).

$$w = \frac{2\pi A_o^2}{\hbar}\left(\frac{e}{2m_o c}\right)^2 M_{cv}\delta(E_c(\mathbf{k}) - E_v(\mathbf{k}) - \hbar\omega) \tag{41}$$

where M_{cv} is the optical element for interband transitions as defined by (28–(32). The notation $|c(\mathbf{k})>$ should here be understood to apply to a quantum well situation. In such case, the index c denotes one of the minibands whose energy lies above the gap while $\mathbf{k}$ refers only to the transverse wave numbers. The index v denotes one of the minibands whose energy lies below the gap.

Transitions can only occur between occupied initial states and empty final states with the same $\mathbf{k}$. In calculating the optical spectra, we will sum over all initial and final states and weight the transitions by the average occupations of the states. The weights are $f_v(\mathbf{k})(1 - f_c(\mathbf{k}))$ for the upward transitions which contribute to the absorption rate w_a and $f_c(\mathbf{k})(1 - f_v(\mathbf{k}))$ for the downward transitions which contribute to emission rate w_e, where $f_c(\mathbf{k})$ and $f_v(\mathbf{k})$ are the occupation factors given below in (46).

The rate of dissipation Q is given by $\hbar\omega(w_a - w_e)/V$, where V is the volume of the part of the heterostructure being considered. Substitution of this expression into (38) and eliminating the electric field, we obtain an expression for the gain g_{act}. In doing this, we also change the summation over $\mathbf{k}$ to an integral.

$$\sum_{\hbar\omega < E_c(k) - E_v(k) < \hbar\omega + d\hbar\omega} 1 = V\rho_{cv}(\hbar\omega)\, d\hbar\omega \tag{42}$$

where ρ_{cv} is the joint density of states of the two minibands. This integration removes the delta function in (39) and the volumes cancel. The final expression for g_{act} is

$$g_{act}(\hbar\omega) = \frac{4\pi^2\alpha_{fs}\hbar^2}{n_{act}\hbar\omega m_o^2}\sum_c\sum_v \rho_{cv} M_{cv}(f_c(\mathbf{k})(1 - f_v(\mathbf{k})) - f_v(\mathbf{k})(1 - f_c(\mathbf{k}))) \tag{43}$$

where $\alpha_{fs} = e^2/\hbar c$ is the fine structure constant. It is understood that $\mathbf{k}$ is selected such that $E_c(\mathbf{k}) - E_v(\mathbf{k}) = \hbar\omega$. If more than one value of $\mathbf{k}$ satisfies this condition, then (43) is understood to be summed over all values of $\mathbf{k}$ so selected.

The above expression for g_{act} shows it to be the difference between contributions of downward and upward transitions.

$$g_{act}(\hbar\omega) = e_{act}(\hbar\omega) - a_{act}(\hbar\omega) \tag{44}$$

where $a_{act}(\omega)$ and $e_{act}(\omega)$ are the coefficients of optical absorption and emission.

We can relate g_{act} to g_{mode} by use of (4.2) and (4.3)

$$\frac{g_{mod}}{g_{act}} = \frac{S_{act}A_{act}}{\int S\, da} \equiv \Gamma_{act}. \tag{45}$$

Γ_{act} is known as the mode occupation factor of the active layers. The mode occupation factors for bulk, multiquantum well and single quantum well lasers are estimated in Table III. They were computed by solving the two-dimensional scalar wave equation by the method of Henry and Verbeek [17] using refractive indices established for the quaternary system [18]. This method is quite similar to the one used here. The optical field is expanded in a two dimensional Fourier sine series converting the scalar wave equation into a matrix eigenvalue equation

B. Computation of the Gain Spectrum

To evaluate g_{act} in (43), we first compute the band structure associated with the quantum well. We calculate all conduction band and valence band dispersion curves for minibands that are likely to be occupied with electrons or holes respectively. Only these minibands can contribute to emission and, hence, to gain. We do this for a number of points (e.g., 30) in k space, taking them in a representative direction, usually the z direction parallel to the plane of the quantum well. Then we calculate the squared matrix elements of each polarization for all the transitions between these states.

To proceed further, we must set the quasi-Fermi levels in the conduction band and valence band. The occupation numbers $f_c(\mathbf{k})$ and $f_v(\mathbf{k})$ are given by

$$f_c(\mathbf{k}) = \frac{1}{\exp\left(\dfrac{E_c(\mathbf{k}) - F_c}{k_B T}\right) + 1}$$

$$f_v(\mathbf{k}) = \frac{1}{\exp\left(\dfrac{E_v(\mathbf{k}) - F_v}{k_B T}\right) + 1} \tag{46}$$

where F_c and F_v are the quasi-Fermi levels and k_B is Boltzman constant.

We find F_c and F_v from the requirement that the average carrier density in the quantum well have specified values n and p. The number of carriers in the quantum well region is found by summing over the bands and weighting their occupations by $f_c(\mathbf{k})$ or $(1 - f_v(\mathbf{k}))$. Just as in the optical transitions, in doing the sum over $\mathbf{k}$, we replace the sum by an integral over a density of states along a representative direction in $\mathbf{k}$ space. The densities of states

TABLE III
MODAL PROPERTIES OF MQW LASERS AT 1.55μm

Type	Number Wells	Well Thickness Å	Strip Width μm	Length μm	Confinement Factor	Interval Mode loss cm^{-1}	Facet Mode Loss cm^{-1}	Threshold Gain of mode cm^{-1}	Active Threshold gain cm^{-1}
bulk	1	1500	0.8	250	0.245	25	48	73	298
MQW	7	80	0.8	250	0.085	20	48	68	796
MQW	4	80	1.0	500	0.039	10	24	34	874
SQW	1	80	2.0	1000	0.0084	5	12	17	2023

depend upon the dimensionality of the **k** summation and will be different in the three-dimensional bulk case and in the two-dimensional quantum well case. In the bulk case the carrier density equals the total number of carriers N divided by the active volume. In a well-designed quantum well laser, the injected carriers will nearly all reside in the active layers. Therefore, in the quantum well case, we compute the carrier density as N divided by the active volume.

The Fermi levels are then set in an iterative procedure by varying them until the specified carrier densities π and p are reached. In the common case of undoped active layers, electrical neutrality requires that $\pi = p_+$. Once the Fermi levels are established, $g_{act}(\hbar\omega)$ can be evaluated with (4.7). The most time-consuming step is solving the eigenvalue problem for all the energy levels and wave functions. Once this is done, it is relatively quick to compute the gain spectra for a set of carrier densities.

C. Broadening of the Gain Spectrum

The optical spectra computed by the procedures described above have sharper features than are seen experimentally. We shall follow the common practice and add an empirical broadening to the spectra by convoluting with a broadening function. It is found that in undoped semiconductors at room temperature, broadening gives rise to a nearly exponential tail on the low energies sides of the absorption and emission edges of the spectrum [19]. This is usually referred to as an Urbach tail. This broadening is thought to be due to interaction with the vibrating lattice. Many body effects may also contribute. In a study of 1.3-μm quaternary lasers, the broadening did not increase very much with carrier injection, indicating that broadening by lattice vibrations may be dominant [19].

If the carriers in each band are in thermal equilibrium, described by a quasi-Fermi level and temperature T, the emission and absorption spectra will be related by an Einstein relation.

$$e_{act}(\hbar\omega) = a_{act}(\hbar\omega) \exp\left(\frac{F_c - F_v - \hbar\omega}{k_B T}\right). \quad (47)$$

The derivation of this formula is outlined below. (It is easy to show that this relation will still hold even if the interaction with the lattice produces phonon side bands, provided that the lattice phonons are also described by the same temperature T.) A consequence of (47) is that the broadening of emission and absorption spectra will be different. For example, if the broadening of absorption is symmetric, the emission will be asymmetric. Experimental studies [18] have verified that the Urbach tail is different in absorption and emission in a way that is predicted by the Einstein relation.

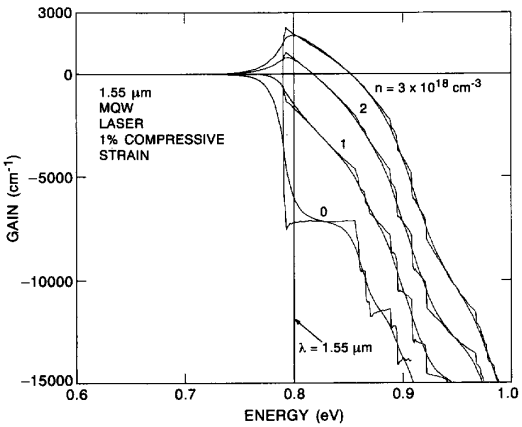

Fig. 3. Optical absorption and gain spectra of a MQW laser with 80 Å wells and barriers. Spectra with and without broadening are compared.

For simplicity, we chose an exponential broadening function which can describe the observed Urbach tails. We broaden the absorption spectrum $a_{act}(\hbar\omega)$ by convolution with the broadening function

$$f_b(x) = \frac{e^{-(|x|/\Delta_b)}}{2\Delta_b}. \quad (48)$$

To be consistent with the Einstein relation, we then calculate $e_{act}(\hbar\omega)$ using (47). The gain spectrum is then given by (44). We used $\Delta_b = 9$ meV, which is consistent with the absorption broadening seen in 1.3 μm quaternary lasers material [18]. The effect of broadening of the absorption and gain spectra of a 1.55 μm MQW laser with compressive strain is shown in Fig. 3. The computation of these spectra is discussed in Section VI.

The Einstein relation follows from the requirement that the optical transition rates be consistent with the results of statistical physics. In a quantum treatment of a laser cavity, the rate of optical absorption is $\sim a_{act}(\hbar\omega)n_{ph}$, where n_{ph} is the photon number. Similarly, the emission rate is $\sim e_{act}(\hbar\omega)(n_{ph} + 1)$ where the 1 is the contribution of spontaneous emission. In the special case of thermal equilibrium, these two rates must be equal. In thermal equilibrium with an excited semiconductor, $F_c - F_v$ is the

chemical potential of the photons [20]. For a Bose gas with this chemical potential, the average level occupation number is

$$n_{ph} = \frac{1}{\exp\left(\dfrac{\hbar\omega - (F_c - F_v)}{k_b T}\right) - 1} \tag{49}$$

which results in the Einstein relation (47).

V. Material Constants

In the following, we calculate absorption and spectral gain for realistic laser structures. We consider laser structures made of the quaternary material system $In_{(1-x)}Ga_xAs_yP_{(1-y)}$ grown on an InP substrate. This is the current material of choice for the fabrication of lasers for communication, since the 1.3μ to 1.55μ wavelength range set by the optical properties of the silica fibers is easily accessed by this choice. This choice has obvious advantages, such as ability to compare calculated results with available experimental data, obtaining insight thereby in the design of new structures. A disadvantage in having to deal with a quaternary mixed crystal system is that the material constants are not very well known; these are required for quantitative modeling of the design and engineering of working devices.

The material constants of the quaternaries are in general a function of their composition (y and x of Fig. 2) and in principle should be measured for each composition. Another approach is to interpolate those constants from the known constants of quaternaries of fixed composition (usually the binaries where x, $y = 0,1$). Interpolation schemes were given by Adachi [21]. The way we have chosen to proceed is slightly different.

Since, in general, the quaternaries are aimed to lattice match the InP substrate, we regard the lattice matched quaternary as if it were composed of the ternary ($In_{0.532}Ga_{0.468}As$) and InP. Thus:

$$In_{1-x}Ga_xAs_yP_{(1-y)} = (In_{0.532}Ga_{0.468}As)_z(InP)_{1-z}. \tag{50}$$

The particular ternary is one which happens to already be lattice matched to InP. By doing this, we generate a line of lattice-matching in the xy composition plane (Fig. 2). Along this line we have:

$$z = y = x/0.468. \tag{51}$$

In this way, we treat the quaternary as being actually a ternary material in the sense that all its properties can be interpolated from the better documented properties of the binary InP and the lattice-matched ternary $In_{0.532}Ga_{0.468}As$. In Table II, we list and reference all the material constants that we use for our calculations. We have made an effort to rely on experimental data rather than calculated numbers wherever possible. All the material constants for the quaternary are linearly interpolated between these of InP and those of $In_{0.532}Ga_{0.468}As$

$$A^Q(z) = (1 - z)A^B + zA^T, \tag{52}$$

where A is one of the material constants, Q stands for the quaternary, B for the binary InP, and T for the lattice matched ternary.

For the quaternary band gap, however, we use parabolic interpolation, to account for the bowing of the bandgap [22].

$$E_g^Q(z) = (1 - z)E_g^B + zE_g^T - z(1 - z)B^Q \tag{53}$$

where $B^Q = 0.012$ eV [22]. Using this equation, we make one to one correspondence between the quaternary room temperature luminescence wavelength and its composition as given by z.

The temperature dependence of the band gap is being calculated using the Varshni phenomenological expression [23]:

$$E_g^Q(T) = E_g^Q(0) - \frac{\alpha T^2}{\beta + T} \tag{54}$$

where T is the temperature in K, $\alpha = 6.9 \times 10^{-4}$ eV/K^2 and $\beta = 327$K. Temkin *et al.* [24] established that these constants hold for a wide range of quaternary materials in addition to InP. We emphasize here that the valence band offset of the quaternary is linearly interpolated between the values of $In_{0.532}Ga_{0.468}As$ ($V_{\text{off}}^T = 0.37$ eV [25]) and that of InP ($V_{\text{off}}^B = 0$). Since the bandgap is interpolated parabolically, this leads to a composition dependent valence band to conduction band offset ratio. The quaternary can be biaxially compressively or tensilely strained by changing its composition from the lattice-matching condition (51). The change in the lattice matching condition is usually done by changing x, *i.e.* moving only the ternary from its lattice matched condition. The amount of change in the group III composition of the quaternary Δx which is needed in order to get a given lattice mismatch strain ϵ is given by:

$$\epsilon = \frac{a^Q(x_{lm}, z) - a^Q(x_{lm} + \Delta x, z)}{a^Q(x_{lm} + \Delta x, z)} \cong -\frac{1}{a^B}\frac{\partial a^Q(x_{lm}, z)}{\partial x}\Delta x \tag{55}$$

where $x_{lm} = 0.468$ and a^Q is the lattice constant of the quaternary, while a^B is the lattice constant of InP. Now using (5.3) for $a^Q(z)$ and similar expression for $a^T(x)$, we get

$$\frac{\partial a^Q(x_{lm}, z)}{\partial x} = z(a_{\text{GaAs}} - a_{\text{InAs}}) \tag{56}$$

substituting back in (5.6) we get:

$$\epsilon = z\frac{a_{\text{InAs}} - a_{\text{GaAs}}}{a_{\text{InP}}}\Delta x \tag{57}$$

The change in composition Δx introduces changes in the material constants. These changes can be calculated in a similar way to the change in the lattice constant:

$$\Delta A^Q(x, z) = \frac{\partial A^Q(x, z)}{\partial x}\Delta x = z(A^{\text{GaAs}} - A^{\text{InAs}})\Delta x \tag{58}$$

where A^{GaAs} and A^{InAs} are the relevant material constants of the binary parents of the ternary, and A^Q is the constant of the quaternary.

The bandgap, which is interpolated parabolically is changed differently:

$$\Delta E_g^Q = z[E_g^{GaAs} - E_g^{InAs} - (1 - 2x_{lm})B^T]\Delta x \quad (59)$$

where the expression in rectangular brackets is simply the partial derivative with respect to x, of (53).

Once the lattice mismatch ϵ is known one can determine all the components of the strain tensor by solving Hooke's Law. In the examples that follow, the direction of growth is (100). In this relatively simple case we get:

$$e_{yy} = e_{zz} = \epsilon;$$

$$e_{xx} = -\frac{2c_{12}}{c_{11}}\epsilon \quad e_{xy} = e_{yz} = e_{zx} = 0 \quad (60)$$

where the x axis is parallel to the growth direction (100).

VI. Modeling of Bulk and Quantum Well Quaternary Lasers

In this section we will apply the computational procedures described above to model bulk and quantum well InGaAsP lasers. We will compare bulk and multiquantum well (MQW) lasers, compare compressively and tensilely strained MQW lasers with unstrained MQW lasers, compare 1.55 μm lasers with 1.3 μm lasers and compare room temperature and high temperature operation. The comparisons are made by calculating the gain spectra and peak gains as a function of carrier density. No attempt will be made to calculate laser currents, for this would require a description of the nonradiative processes.

It should be borne in mind that these calculations are quantitative but not exact. The spectra were phenomologically broadened in a way that corresponds with observations made on 1.3 μm lasers at room temperature. Increased broadening with carrier injection or temperature was not introduced. Coulomb interaction between electrons and holes, which results in the formation of excitons at low carrier density, was neglected. Changes in the potential wells resulting from the distribution of injected carriers are not calculated. Changes in mode occupation due to changes in refractive index of the active layer caused by carrier injection were neglected. The quaternary band parameters were estimated by linear extrapolation of parameters of InP and the lattice matched ternary materials. Despite these disclaimers, we expect that our calculations give a nearly quantitative description of real lasers and that the trends we find should be borne out by experimental observations.

Multiquantum well (MQW) lasers usually have four to 10 wells. Increasing the number of wells serves mainly to increase the mode occupation factor (fraction of optical power in the active area) and does not significantly change $g_{act}(n)$, the gain within the active layer as a function of carrier density n. Therefore, we simulated the MQW lasers by calculating a superlattice, which represents an infinite number of wells and calculated $g_{act}(n)$ of a single active layer (well). This required fewer Fourier waves because the envelope functions only had to be calculated for one period of the structure. In the illustrations that follow, we used 80 Å wells separated by 80 Å barrier layers. The period of the superlattice was $X = 160$ Å. The wells were in the y-z plane. The quantum well wave functions were expanded in a Fourier series in the x direction. We usually use 11 waves (values of k_x). The computed gain spectrum was found to be negligibly altered when the number of waves was increased from 11 to 13.

The basis states used were products of the 11 waves and 8 zone center Bloch functions. Thus the matrix to be diagonalized is of order 88. This matrix had to be solved for each occupied point in the Brillouin zone (BZ). We simulated the relevant section of the BZ by 30 points in the z direction. A thorough simulation should take other directions in the yz plane. It was shown, however, by Gershoni *et al.* [26] that this direction, which is at 45° relative to the electric field of the electromagnetic radiation in the laser cavity, is an excellent approximation for the average over all directions in the quantum well plane yz. To simulate the superlattice we repeated the calculations with $k_x = (2\pi/X)(j + q_x)$ where $(2\pi/X)\ q_x$ is the wave vector describing propagation in the superlattice. The calculation was repeated for six values of q_x spanning the range of $-(1/2)$ to $1/2$ Therefore the eigenvalues had to be solved $6 \times 30 = 180$ times. This computation took about 20 minutes on a Sun workstation and about 2 minutes on a Cray computer. Another 8 minutes of computation on a Sun work station was needed to calculate the gain spectrum for 8 values of carrier density. In Fig. 3 we display absorption and gain spectra of 1.55 μm MQW laser, subject to 1% compressive strain. Spectra with and without broadening are displayed for four different carrier densities.

Computation of the bulk laser consisted of expanding the wave function in the 8 zone center Bloch functions with only one Fourier wave $k_x = 0$, in the x direction. The transverse BZ was simulated by $\mathbf{k}$ in the x, y, and z directions, using 50 points in each direction. This computation takes less than $1/10$ the time for simulating a quantum well laser (see Fig. 1).

A. Comparison of Bulk and Quantum Well Lasers at 1.55 μm

Let us begin by comparing bulk lasers with quantum well lasers having compressive strain. As we discuss below, of the various quantum well lasers that we considered, those with compressive strain are expected to have the lowest threshold carrier densities and highest differential gains.

Fig. 4 shows the gain spectrum of a bulk laser operating near 1.55 μm. As in all of our examples, the gain is that within the active layer g_{act}, not the mode gain g_{mode}. The horizontal lines in the figure are the typical threshold values of g_{act} expected for bulk, multiquantum well (MQW) and single quantum well (SQW) lasers. Laser threshold is

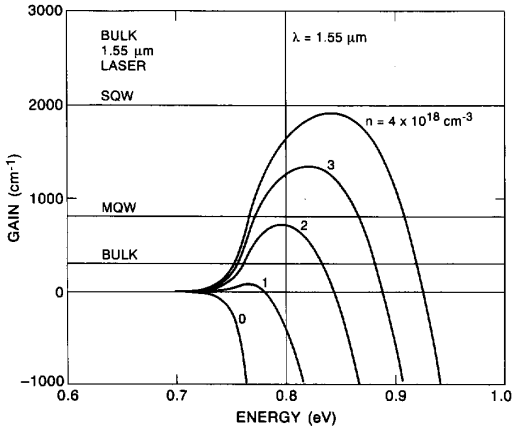

Fig. 4. Gain spectra of a bulk 1.55 μm laser. The horizontal lines are the active layer gains required to reach threshold for bulk, MQW and SQW lasers.

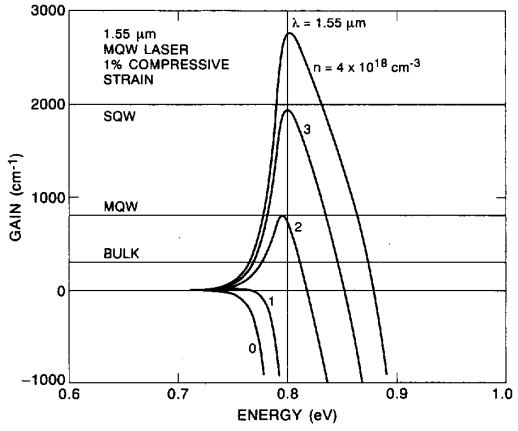

Fig. 5. Gain spectra of a MQW 1.55 μm laser with 1% compressive strain.

reached when the g_{mode} is equal to the modal loss. These threshold gains are detailed in Table III. The horizontal lines are equal to g_{act} at threshold given by g_{mode} at threshold divided by Γ_{act}, where Γ_{act} is the active layer occupation factor of the mode. Similar values of g_{act} at threshold are found for 1.3 μm lasers. The peak gain moves to higher optical energy with increasing carrier density n. This shift occurs because for a bulk laser the joint density of states increases approximately as $(\hbar\omega - E_g)^{1/2}$. As the bands fill with carriers, higher lying densities of states become inverted and the peak gain moves to higher optical energy. In the case of a quantum well, the joint density of states associated with the optical transitions is nearly independent of energy, increasing (in the absence of broadening) in a step-like manner. This is evident in the optical absorption spectrum of Fig. 3. Consequently, peak gain occurs at a fixed optical energy until the second quantum well transition becomes inverted, then an abrupt shift in the wavelength of peak gain should occur. Broadening of the optical transitions causes this shift to occur a little more gradually. The gain spectrum for the compressively strained quantum well laser is shown in Fig. 5. Only a slight shift in the optical energy of peak gain occurs.

The peak gains of the bulk and compressively strained MQW lasers are plotted versus carrier density n in Fig. 6. We see that the bulk laser achieves positive gain at lower carrier density, but the gain of the MQW laser increases more rapidly with increasing carrier density.

In comparing bulk and quantum well lasers and comparing quantum well lasers of different designs, we are faced with the difficulty of comparing lasers with similar modes, but very different active volumes V_{act}. Consider the threshold condition of a Fabry–Perot laser.

$$g_{mode}L - \gamma_{mode}L = \ln \frac{1}{\sqrt{R_1R_2}} \tag{61}$$

where L is the length of the laser, R_1 and R_2 are the facet power reflectivities and γ_{mode} is the internal loss. For different lasers, the amplification $g_{mode}L$ must be nearly the same at threshold. We assume that different lasers have similar mode areas A_{mode}. Then

$$g_{mode}L = \frac{g_{act}A_{act}L}{A_{mode}} \sim g_{act}V_{act}. \tag{62}$$

The loss $\gamma_{mode}L$ due to optical absorption by electrons and holes is given by

$$\gamma_{mode}L = \frac{d\gamma}{dn}\frac{nA_{act}L}{A_{mode}} \sim nV_{act}. \tag{63}$$

The threshold current I is given by

$$I = \frac{enA_{act}L}{\tau(n)} \sim \frac{nV_{act}}{\tau(n)}. \tag{64}$$

We see that to compare different lasers, we must multiply both g_{act} and n in Fig. 6 by V_{act}. The curves will change in scale, but not in shape. Notice that the slopes of the straight lines radiating from the origin in Fig. 6 are unchanged by these multiplications. These slopes are proportional to the amplification per injected carrier A/N,

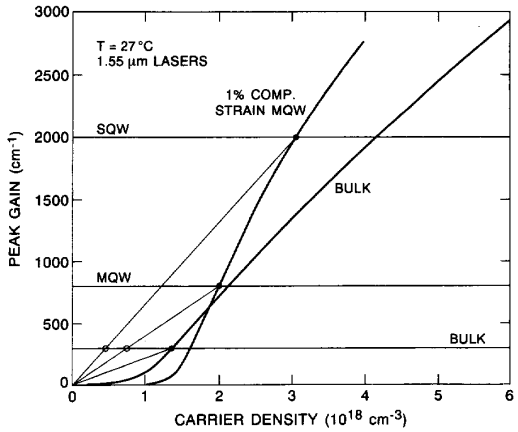

Fig. 6. Peak active layer gain g versus carrier density for bulk and 1% compressively strained lasers operating at 1.55 μm versus carrier density n within the active layer. The slopes of the lines from the origin are proportional to A/N. The circles on the bulk loss line show the relative carrier numbers at threshold.

where $A = g_{mode}L \sim g_{act}V_{act}$ and $N = nV_{act}$. Multiplying g_{act} and n by V_{act} transforms the plots in Fig. 6 into a plot of A versus N. Since the A of each laser is nearly the same at threshold, N at threshold diminishes as A/N (slope of the straight line) increases. The horizontal positions of circles in Fig. 6 along the bulk laser threshold line show the relative values of N at threshold for the bulk, MQW and SQW lasers.

Fig. 6 illustrates that the amplification per injected carrier A/N progressively increases as we go from bulk, to MQW, to SQW lasers. As V_{act} decreases, the laser operates at higher levels of inversion, a smaller fraction of the injected carriers are used merely to reach transparency and A/N increases. In addition, the MQW lasers are an improvement over bulk because of the confinement of the carriers in the bands to two dimensions instead of three and because of reduced hole band masses in some cases.

The loss of the mode due to absorption of light by free electrons and intervalence band absorption by holes is proportional to N (63). The reduction of N in MQW and SQW lasers results in the remarkably high efficiency of these lasers [27], [28]. The reduction of threshold current I in going from bulk to a MQW laser will be less pronounced than the reduction in loss, because the quantum well laser operates at higher carrier density than bulk laser and the carrier lifetime $\tau(n)$ in (64) is reduced.

B. Comparison of Bulk, MQW and Ideal MQW lasers

In Figs. 7 and 8, we plot the peak gains versus carrier density for bulk and MQW lasers having 1% compressive strain, no strain and 1% tensile strain. These lasers are designed to operate near 1.55 μm at 27°C. The calculations in Fig. 7 are at 27°C and in Fig. 8 are at 87°C. In addition, we show curves for an "ideal" MQW laser, which we discuss below. The curves indicate that compressively strained MQW lasers are considerably better than unstrained and tensile strained lasers. Tensile strained MQW lasers appear to be somewhat worse than unstrained MQW lasers. The curves have nearly the same relations to one another at 87°C as at 27°C. All of the quantum well lasers have better A/N slopes than the bulk laser. This indicates that quantum well lasers are generally more efficient than bulk lasers in part due to their smaller active volumes.

In a bulk laser, the carriers spread out three dimensionally to fill the bands in k space. Roughly speaking, to maintain a given level occupation, the carrier density will have to increase as $(k_BT)^{3/2}$ due to the spreading of carriers in the bands. In a quantum well laser, the spreading in k space is restricted to two dimensions. Ideally then, the carrier density will increase as (k_BT) due to the spreading of carriers in the mini-bands. However, there are many miniband associated with the various bound and unbound levels of the quantum well. The quantum well laser behaves ideally only if the levels are sufficiently well separated that only lowest conduction miniband and highest valence miniband are occupied. Only these levels contribute to the lasing transition.

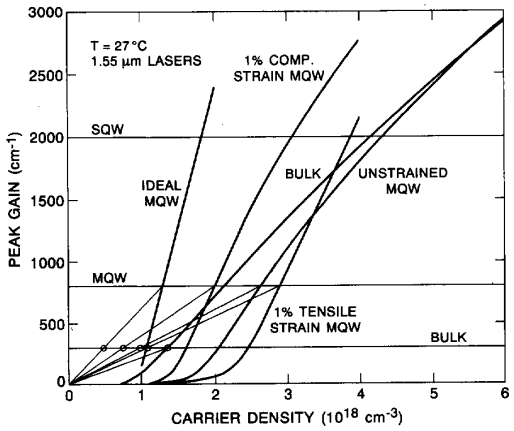

Fig. 7. Peak active layer gain g versus carrier density n for bulk, 1% compressively strained, 1% tensilely strained and unstrained MQW 1.55 μm lasers at 27°C. The fictitious "ideal" case of a laser with 1% compressive strain and occupation of only the uppermost valence band and lowermost conduction band is also shown. The circles on the bulk loss line compare the relative carrier numbers N at threshold.

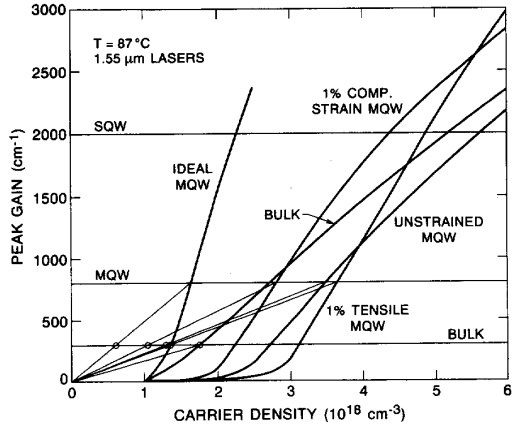

Fig. 8. Peak active layer gain g versus carrier density n for bulk, 1% compressively strained, 1% tensilely strained, unstrained and "ideal" MQW 1.55 μm lasers at 87°C. The circles on the bulk loss line compare the relative carrier numbers N at threshold.

The "ideal" quantum well behavior shown in Figs. 7 and 8 was simulated by only populating the lowest conduction miniband and highest valence miniband of a compressively strained quantum well laser. The "ideal" laser has a behavior that is much superior to that of the real quantum well laser, because in real MQW lasers the carriers, particularly the holes, occupy other bands. These carriers contribute nothing to the lasing transition, but they do contribute to radiative and Auger recombination.

Figs. 9 and 10 show the band structure of the conduction bands and valence bands of 1.55 μm lasers with a) 1% compressive strain, b) no strain, and c) 1% tensile strain. The short horizontal lines in these figures show the band edges of the bulk material. The long horizontal lines in these figures show the energies associated with 90%, 50% and 1% occupation. The Fermi levels are the lines of 50% occupation. These occupations were calculated

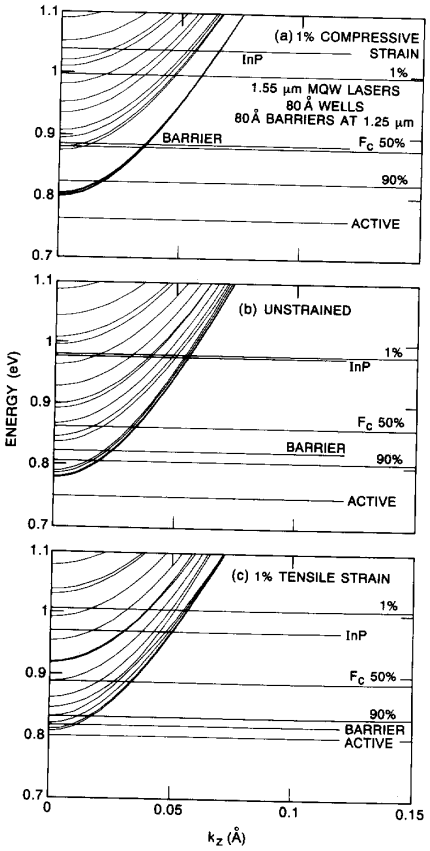

Fig. 9. Comparison of the conduction band structure for 1% compressively strained, unstrained and 1% tensilely strained 1.55 μm MQW lasers.

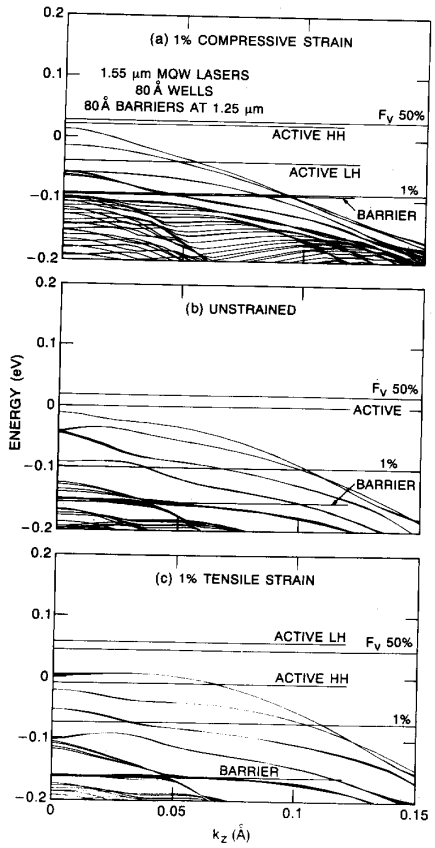

Fig. 10. Comparison of the valence band structure for 1% compressively strained, unstrained and 1% tensilely strained 1.55 μm MQW lasers.

for $n = 3 \times 10^{18}$ cm^{-3} at 27°C. We see in Fig. 9 that as we go progressively from compressive to tensile strain, the confinement of electrons within the well is reduced. The position of the Fermi level in Fig. 9 shows that there is a substantial occupation of higher conduction bands, even in the case of compressive strain.

The most striking difference in the valence bands in Fig. 10 is that the band mass of the uppermost valence band is much smaller for compressive strain than for tensile strain. This is probably the most important factor in making compressively strained lasers superior to tensile strained lasers.

In a bulk laser, most of the holes occupy the heavy hole band and the light and heavy hole bands are degenerate at $\mathbf{k} = 0$ (Fig. 2). In an unstrained quantum well laser, this degeneracy is removed by the spatial quantization which splits the light and heavy hole levels at $\mathbf{k} = 0$, due to their effective mass difference for motion normal to the quantum well plane. This splitting of the heavy hole levels above the light hole levels is enhanced by compressive strain. On the other hand, the splitting is reduced and reversed with tensile strain. Tensile strain also reverses the normal polarization of the lasing mode, the peak gain occurring for TM polarization instead of TE. The heavy hole level receives its name from the heavy hole associated with motion within the quantum well (normal to the quantum well plane). However, it has a light hole mass for motion parallel to the plane and this is the mass that controls carrier density. Thus compressive strain enhances occupation of hole bands with light hole mass, while tensile strain enhances occupation of hole bands with heavy mass. These beneficial effects of compressive strain were recognized in the early papers of Adams [29] and Yablonovitch and Kane predicting the effect [30].

This effect is quite evident in Fig. 10. Comparing Figs. 10(a) and (c), we see that the uppermost hole band has a much greater curvature in the case of compressive strain than in the case of tensile strain and hence, tensile strain requires a greater number of holes to achieve the same occupancy of this band near $\mathbf{k} = 0$. The unstrained laser lies somewhat between these two extremes.

C. Bulk and MQW Lasers at 1.3 μm

We now turn to a comparison of bulk and quantum well lasers operating at 1.3 μm. Figs. 11–14 show the active layer gain versus carrier density at 27°C and 87°C and the conduction band and valence band dispersion curves for 1.3 μm lasers. They can be compared with the corresponding Figs. 7–10 for 1.55 μm lasers.

Comparing Figs. 7 and 11, we see that even for bulk

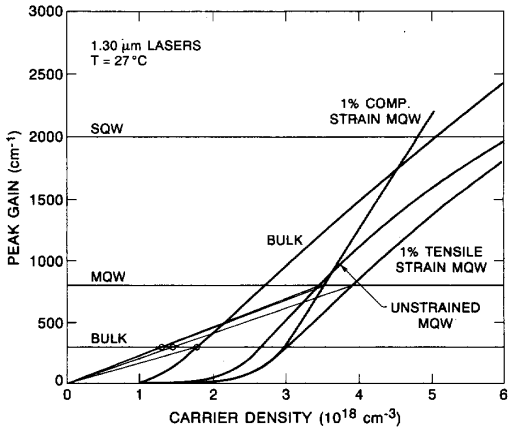

Fig. 11. Peak active layer gain g versus carrier density n for bulk, 1% compressively strained, 1% tensilely strained and unstrained MQW 1.30 μm lasers at 87°C. The circles on the bulk loss line compare the relative carrier numbers N at threshold.

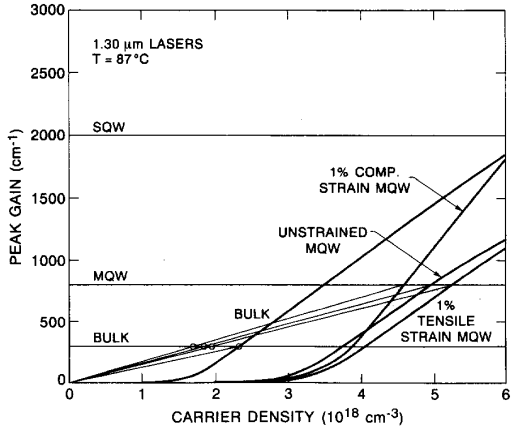

Fig. 12. Peak active layer gain g versus carrier density n for bulk, 1% compressively strained, 1% tensilely strained and unstrained MQW 1.30 μm lasers at 87°C. The circles on the bulk loss line compare the relative carrier numbers N at threshold.

lasers, somewhat higher carrier densities are required to achieve threshold. This is probably due to the slightly higher band masses and smaller optical matrix element for the 1.3 μm laser materials compared to the 1.55 μm laser materials.

Fig. 11 and 12 plotting gain versus carrier density for 1.3 μm show that the MQW lasers require considerably higher carrier densities than bulk lasers. Among the quantum well lasers, the compressively strained MQW laser is still superior, but it does not stand out from the others as much as it does at 1.55 μm. Its main advantage appears to be higher differential gain. The probable reason for the drop in performance of the quantum well lasers relative to bulk at 1.3 μm is that well confinement is reduced at this wavelength. For both the valence band and conduction band, the energy separations between the active layer and barrier layer are reduced for the 1.3 μm laser as shown

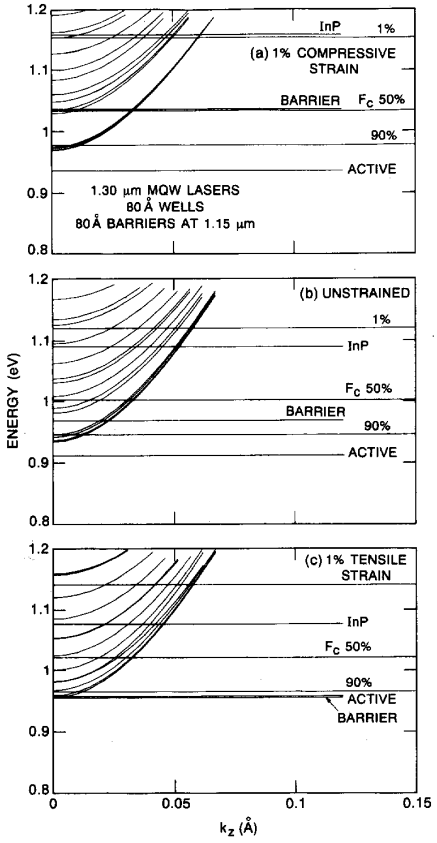

Fig. 13. Comparison of the conduction band structure for 1% compressively strained, unstrained and 1% tensilely strained 1.30 μm MQW lasers.

in Fig. 13 and 14. The shallower wells and higher band masses reduce the separations between the quantum well energy levels and hence the confinement of carriers in the lasing bands. Despite the diminished advantage of quantum well lasers relative to bulk lasers at 1.3 μm, the slopes

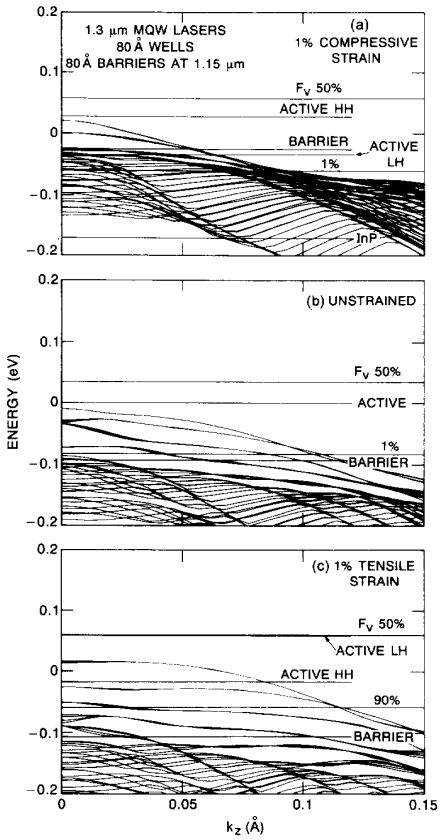

Fig. 14. Comparison of the valence band structure for 1% compressively strained, unstrained and 1% tensilely strained 1.30 μm MQW lasers.

of the straight lines in Figs. 11 and 12 indicate that quantum well lasers should still have slightly lower internal losses than bulk lasers at this wavelength due to their smaller active volume.

VII. Summary and Discussion

We have described a program for calculating the electronic states and optical properties of heterostructures in semiconductors. The program was applied to the study of bulk and strained MQW lasers. A curve of peak gain versus carrier density could be generated in less that 30 minutes of computation on a Sun work station. The program was particularly suited to modeling periodic structures, but it could also be used to model QW lasers with one or a few wells. For modeling MQW lasers with more than four wells, a superlattice model was used. The envelope functions only need to be computed for a single period of the superlattice and this requires far fewer waves in the Fourier expansion.

It was found that the MQW lasers were far from ideal owing to the occupation of the closely spaced minibands. This occupation leads to inefficiency because only the uppermost valence band and the lowest conduction band contribute to gain, while all the occupied bands contribute to recombination. Despite this nonideality, MQW lasers were found to have higher amplification per injected carrier than bulk lasers at both 1.55 and 1.3 μm. This results in lasers with high differential quantum efficiency, a property for which MQW lasers are known to excel. The high amplification per carrier is a consequence of the smaller active volume of the MQW lasers which requires fewer carriers to reach transparency and also due to the confinement in one dimension. This is particularly true for compressively strained MQW lasers which have the best performance.

The advantage of compressive strain is that hole miniband associated with the lasing transition has a relatively low effective mass. Another lesser advantage is that the well depth for confining the electrons is deeper with compressive strain. MQW lasers with compressive strain had significantly higher differential gains both at 1.55 and 1.3 μm. This should result in higher modulation speeds of MQW lasers than bulk lasers.

The main disadvantage of MQW lasers is that they operate at higher carrier densities than bulk lasers. This is especially true at 1.3 μm. The shallower wells of MQW lasers operating at 1.3 μm made them even less ideal than at 1.55 μm. In view of the suspected importance of the Auger recombination in determining the high temperature performance of long wavelength semiconductor lasers, the lower threshold density of bulk lasers at 1.3 μm may be an advantage.

Acknowledgment

The authors thank T. Tanbun-Ek, H. Temkin, and W. D. Johnston, Jr., for helpful discussions.

References

[1] E. O. Kane, "Energy Band Theory," in *Handbook on Semiconductors*, vol. 1, W. Paul, Ed. Amsterdam, North Holland, 1982, pp. 193–217.

[2] G. Bastard and J. A. Blum, "Electronic states in semiconductor heterostructures," *IEEE J. Quant. Electron.*, vol. QE-22, pp. 1625–1644, 1986.

[3] G. A. Baraff and D. Gershoni, "Eigenfunction-expansion method for solving the quantum wire problem: Formulation," *Phys. Rev.* vol B43, pp. 4011–4022, 1991.

[4] J. Bardeen and W. Shockley, "Deformation potentials and mobilities in nonpolar crystals," *Phys. Rev.* vol. 80, pp. 72–80 1950.

[5] S. W. Corzine, R. Yan, and L. A. Coldren, "Optical gain in III-V bulk and quantum well semiconductors," in *Quantum Well Lasers*, P. Zory, Ed. New York: Academic Press, (to be published).

[6] J. P. Loehr and J. Singh, "Theoretical studies of the effect of strain on the performance of strained quantum well lasers based on GaAs and InP technology," *IEEE J. Quant. Electron.*, vol. 27, p. 708, 1991.

[7] J. Callaway, *Energy Band Theory*. New York: Academic Press, 1964.

[8] D. L. Smith and C. Mailhiot, "Theory of superlattice electronic structure," *Revs. of Mod. Physics*, vol. 62, pp. 173–234, 1990.

[9] J. N. Schulman and Y.-C. Chang, "Reduced Hamiltonian method for solving the tight-binding model of interfaces," *Phys. Rev.*, vol. B27, pp. 2346–2354, 1983.

[10] P. C. Sercel and K. J. Vahalla, "Analytical Formalism for Determining Quantum-Wire and Quantum Dot Band Structure in the Multiband Envelope Function Approximation," *Phys. Rev.* vol. B42, pp. 3690–3710, 1990.

[11] J. M. Luttinger, "Quantum Theory of Cyclotron Resonance in Semiconductors: General Theory," *Phys. Rev.*, vol. 102, pp. 1030–1041, 1956.

[12] G. E. Pikus and G. L. Bir, "Effect of Deformation on the Hole Energy Spectrum of Germanium and Silicon," *Fiz. Tverd. Tela* vol. 1, pp. 1642–1658, 1959 [Sov. Phys. Solid State vol. 1, pp. 1502–1517, 1960].
[13] Thomas B. Bahder, "Eight-band **k** · **p** Model of Strained Zinc-Blende Crystals," *Phys. Rev.* vol. B41, pp. 11992–12001, 1990.
[14] M. Cardona and N. E. Christensen, "Acoustic Deformation Potentials and Heterostructures Band Offsets in Semiconductors," *Phys. Rev.* vol. B35, pp. 6182–6194, 1987 and references therein.
[15] L. I. Schiff, "*Quantum Mechanics*," McGraw-Hill, New York (1968) 3rd Ed., p. 285.
[16] B. T. Smith, J. M. Boyle, J. J. Dongarra, B. S. Garbow, Y. Ibebe, V. C. Klema and C. B. Moler, *Matrix Eigensystem Routines-EISPACK Guide*. New York: Springer 1976.
[17] C. H. Henry and B. H. Verbeek, "Solution of the Scalar Wave Equation for Arbitrarily Shaped Waveguides by Two Dimensional Fourier Analysis," *J. of Lightwave Technology*, vol. 7, pp. 308–313 1989.
[18] C. H. Henry, L. F. Johnson, R. A. Logan, D. P. Clarke, "Determination of the refractive index of InGaAsP epitaxial layers by mode line luminescence spectroscopy," *IEEE J. Quant. Electron.*, vol. QE-21, p. 1887, 1985.
[19] C. H. Henry, R. A. Logan, H. Temkin, F. R. Merritt, "Absorption, emission and gain Spectra of 1.3 micron InGaAsP Quaternary Lasers," *IEEE J. of Quant. Elect.*, vol. QE-19, p. 941, 1983.
[20] C. H. Henry, R. A. Logan, and F. R. Merritt, "Measurement of gain and absorption spectra in AlGaAs buried heterostructure lasers," *J. Appl. Phys.*, vol. 51, pp. 3042–3050, 1980.
[21] S. Adachi, "Material parameters of $In_{1-x}Ga_xAs_yP_{1-y}$ and related binaries," *J. Appl. Phys.*, vol. 53, pp. 8775–8792, 1982.
[22] R. E. Nahory, M. A. Pollack, W. D. Johnston Jr., and R. L. Borus, "Band gap versus composition and demonstration of Vegards Law for $In_{1-x}Ga_xAs_yP_1$ lattice matched to Inp," *Appl. Phys. Lett.*, vol. 33, pp. 659–651, 1978.
[23] Y. P. Varshni, "Temperature dependence of the energy gap in semiconductors," *Physica*, vol. 34, pp. 149–154, 1967.
[24] H. Temkin, V. G. Keramidas, M. A. Pollack, and W. R. Wagner, "Temperature dependence of photoluminescence of n-InGaAsP," *J. Appl. Phys.* vol. 52, pp.1574–1578, 1981.
[25] S. R. Forrest, P. H. Schmidt, R. B. Wilson and M. L. Kaplan, "Relationship between the conduction-band discontinuities and band-gap differences of InGaAsP/heterojunctions," *Appl. Phys. Lett.*, vol. 45, pp. 1199–1201, 1984.
[26] D. Gershoni, I. Brener, G. A. Baraff, S. N. G. Chu, L. N. Pfeiffer, and K. West, "Anisotropy in the interband transitions of (110) oriented quantum wells," *Phys. Rev.*, vol. B44 p. 1930, 1991.
[27] D. Coblentz, T. Tanbun-Ek, R. A. Logan, A. M. Sergent, S. N. G. Chu and P. S. Davisson, "Strained multiple quantum well lasers emitting at 1.3 μm grown by low-pressure metalorganic vapor phase epitaxy," *Appl. Phys. Lett.*, vol. 59, pp. 405–407, 1991.
[28] H. Temkin, N. K. Dutta, T. Tanbun-Ek, R. A. Logan and A. M. Sergent, "InGaAs/InP quantum well lasers with sub-mA threshold current," *Appl. Phys. Lett.*, vol. 57, pp. 1610–1612, 1990.
[29] A. R. Adams, *Electron. Lett.*, vol. 22, p. 249, 1986.
[30] E. Yablonovitch and E. O. Kane, *IEEE J. Lightwave Technol.*, vol. LT-4, p. 504, 1986.

D. Gershoni, photograph and biography not available at the time of publication.

C. H. Henry, photograph and biography not available at the time of publication.

G. A. Baraff, photograph and biography not available at the time of publication.